Orbits, spirals, and trapped states: Dynamics of a phoretic Janus particle in a radial concentration gradient

Parvin Bayati[†] and Stewart A. Mallory[*,†,‡]

[†]*Department of Chemistry, The Pennsylvania State University, University Park, Pennsylvania, 16802, USA*

[‡]*Department of Chemical Engineering, The Pennsylvania State University, University Park, Pennsylvania, 16802, USA*

E-mail: sam7808@psu.edu

Abstract

A longstanding goal in colloidal active matter is to understand how gradients in fuel concentration influence the motion of phoretic Janus particles. Here, we present a theoretical description of the motion of a spherical phoretic Janus particle in the presence of a radial gradient of the chemical solute driving self-propulsion. Radial gradients are a geometry relevant to many scenarios in active matter systems and naturally arise due to the presence of a point source or sink of fuel. We derive an analytical solution for the Janus particle's velocity and quantify the influence of the radial concentration gradient on the particle's trajectory. Compared to a phoretic Janus particle in a linear gradient in fuel concentration, we uncover a much richer set of dynamical behaviors, including circular orbits and trapped stationary states. We identify the ratio of the phoretic mobilities between the two domains of the Janus particle as a central quantity in tuning their dynamics. Our results provide a path for developing novel protocols for tuning the dynamics of phoretic Janus particles and mixing fluid at the microscale. In addition, this work suggests a method for quantifying the surface properties of phoretic Janus particles, which have proven challenging to probe experimentally.

Introduction

Phoretic Janus particles are a novel class of colloids that show promise for applications related to mixing, sorting, and chemical delivery.[1–4] These typically micron-sized particles self-propel due to their unique ability to generate and sustain chemical gradients across their surface.[5,6] The particles' Janus nature, where their surface is composed of two chemically distinct regions, is a common design feature for introducing self-propulsion. Experimentally, it is possible to tune both the size and composition of these regions, and there now exists a sizeable catalog of phoretic Janus particles, including bimetallic and platinum-coated colloids, biodegradable Janus micromotors, and colloidal particles coated in two different enzymes.[7–17] An appropriate fuel source is a second design element nearly universal to these systems. Hydrogen peroxide is a popular choice as one of the particle regions is usually metallic and catalytic. However, the fuel choice is flexible depending on the particle's composition. For example, enzyme-coated particles use the corresponding substrate as the fuel source.[18] With their diverse compositions and fuel sources, phoretic Janus particles offer a robust design platform for engineering behavior at the microscale.

Notably, the ability of these particles to autonomously navigate complex microfluidic environments makes them an ideal candidate for a range of chemical delivery and sensing applications, including targeted drug delivery and environmental remediation .[19–30] For example, recent *in situ* work shows $CaCO_3$ Janus particles exhibit a pH sensitivity that can induce a chemotactic response toward HeLa cancer cells.[31] Regarding environmental remediation, Wang et al.[28] recently proposed a strategy for removing microplastics using photocatalytic TiO_2 Janus particles. Additionally, phoretic Janus can serve as a tool for fluid mixing and directing self-assembly at the microscale.[32,33] Examples include restructuring colloidal gels by incorporating a small fraction of phoretic Janus particles into the gel network,[34–37] powering primitive micromachines,[38–40] and generating bulk fluid flow by fabricating self-pumping walls patterned with Janus micropillar arrays[41] or by trapping phoretic Janus particles near boundaries or surfaces.[42,43]

Any application utilizing phoretic Janus particles requires a deep understanding of how they explore and respond to their environment. A ubiquitous feature of these systems is the role of gradients in chemical fuel concentration, which can dramatically affect their single particle and collective behavior.[44–60] Several studies have focused on the behavior of a single phoretic Janus particle in a linear fuel concentration gradient and shown phoretic Janus particles will undergo a chemotactic response where the particle will reorient to move parallel or anti-parallel to the gradient.[61–64] However, the characterization of the motion of phoretic Janus particles in chemical gradients of other geometries is limited. A critical case that has received lesser attention and the focus of this study is radially symmetric gradients generated from the presence of a point sink or source of the chemical fuel self-propelling the particle.

Using a combination of analytical theory and numerical simulation, we quantify the influence of the radial concentration field on the Janus particle's trajectory. The particle can exhibit a rich array of behaviors that strongly depend on its surface properties, initial configuration, and the strength of the sink or source. The particle can migrate toward or away from the sink or source, similar to a passive particle in an external chemical gradient. In addition, we identify conditions that trap the particle in a stationary state at a fixed distance from the sink or source. Furthermore, the particle's motion is no longer rectilinear as in the case of a particle in a linear fuel concentration gradient but can undergo a spiraling motion. We identify conditions that stabilize the spiraling trajectories leading to a circular orbit about the sink or source. As stationary and orbiting states offer an innovative way to blend and pump fluid continually, our findings suggest potential applications in fluid mixing and

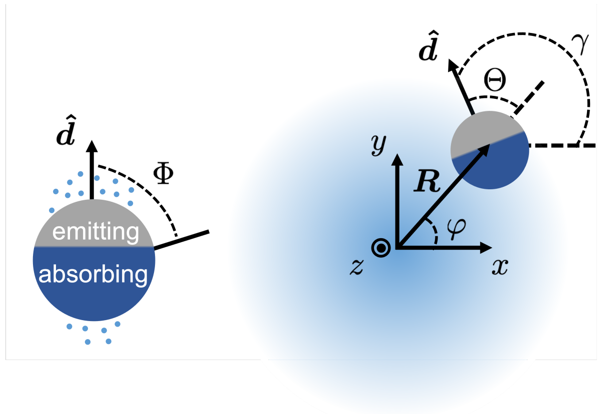

Figure 1: Schematic of a spherical Janus particle with Janus balance $\chi = -\cos\Phi$ immersed in solution near a source or sink of the same chemical solute driving self-propulsion. The distance of the particle from the source R and its orientation $\Theta = \cos^{-1}(\hat{\boldsymbol{R}} \cdot \hat{\boldsymbol{d}})$ fully specify the particle configuration.

microscale transport. In addition, the characteristic dynamics of a phoretic Janus particle in the presence of a point sink or source can serve as a diagnostic tool to identify its surface properties, which has been an experimental challenge.

Model System – We consider a phoretic Janus particle of diameter a with bilateral symmetry along a predefined orientation unit vector $\hat{\boldsymbol{d}}$ as shown in Fig. 1. We implement a standard generic model for the phoretic self-propulsion mechanism where one region of the particle (gray) emits a particular chemical solute and the other region absorbs the solute (blue).[65,66] The chemical solute represents the fuel driving self-propulsion. The relative ratio of the absorbing to the emitting region is defined via the Janus balance χ such that a half-covered particle has $\chi = 0$, a particle emitting solute over its entire surface has $\chi = 1$, and for a fully absorbing particle $\chi = -1$. To preserve mass balance, the rate of emission Q_e and absorption Q_a of the solute are constant, and there is no net change of solute such that $S_e Q_e - S_a Q_a = 0$, where S_e and S_a are the surface areas of the emitting and absorbing regions of the particle, respectively. Under these steady-state conditions, a simple relationship exists between the emission and absorption rates of the two regions and the Janus balance χ given by $Q_a/Q_e = (1+\chi)/(1-\chi)$.

Here, we focus on the athermal low Reynolds number limit, where Brownian motion is negligible, and particle motion is dominated solely by the phoretic self-propulsion mechanism. In this regime, the particle's motion is deterministic and, as we demonstrate, confined to a two-dimensional plane. The position of the particle relative to the source is given by a vector $\boldsymbol{R} = R\cos\varphi\,\hat{\boldsymbol{x}} + R\sin\varphi\,\hat{\boldsymbol{y}}$ where R is the radial distance from the source and φ is the angle between $\boldsymbol{R}$ and the positive x-axis as shown in Fig. 1. We obtain the trajectory of the particle by integrating the equations of motion:

$$\frac{dR}{dt} = U_R \tag{1a}$$

$$\frac{d\varphi}{dt} = \frac{U_\varphi}{R} \tag{1b}$$

$$\frac{d\gamma}{dt} = \Omega_z \tag{1c}$$

where $U_R = \boldsymbol{U}\cdot\hat{\boldsymbol{R}}$ and $U_\varphi = \boldsymbol{U}\cdot\hat{\boldsymbol{\varphi}}$ are the radial and tangential components of the translation velocity $\boldsymbol{U}$, respectively. The corresponding radial and tangential unit vectors are given by $\hat{\boldsymbol{R}} = \cos\varphi\,\hat{\boldsymbol{x}} + \sin\varphi\,\hat{\boldsymbol{y}}$ and $\hat{\boldsymbol{\varphi}} = \hat{\boldsymbol{z}}\times\hat{\boldsymbol{R}} = -\sin\varphi\,\hat{\boldsymbol{x}} + \cos\varphi\,\hat{\boldsymbol{y}}$, respectively. The orientational dynamics of the particle are given by Eq. (1c) where γ is the angle between the orientation vector $\hat{\boldsymbol{d}}$ and the positive x-axis and Ω_z is the only nonzero component of the angular velocity of the particle. It is useful to define an auxiliary angle $\Theta = \gamma - \varphi$ which is the angle between $\hat{\boldsymbol{R}}$ and the orientation vector $\hat{\boldsymbol{d}}$, and from Eq. (1b,c) it follows that $d\Theta/dt = d\gamma/dt - d\varphi/dt = \Omega_z - U_\varphi/R$. A particle's configuration relative to the singularity is fully specified by Θ and $\boldsymbol{R}$.

The Stokes equations prescribe the dynamics of the fluid and are given by

$$\eta\nabla^2\boldsymbol{u} - \nabla p = 0 \tag{2a}$$

$$\nabla\cdot\boldsymbol{u} = 0 \tag{2b}$$

where η, $\boldsymbol{u}$ and p are the dynamic viscosity, fluid velocity, and pressure, respectively. In the laboratory frame, the boundary conditions are $\boldsymbol{u} = 0$ at infinity and on the surface of the particle $\boldsymbol{u} = \boldsymbol{U} + \boldsymbol{\Omega} \times (\boldsymbol{r} - \boldsymbol{r}_0) + \boldsymbol{u}_s$ where $\boldsymbol{u}_s$ is the slip velocity of the fluid at the particle's surface. Using the force and torque-free condition on the particle and the Lorentz reciprocal theorem,[67] the translation and angular velocity of a particle in an unbounded domain are[68]

$$\boldsymbol{U} = -\frac{1}{4\pi a^2} \int_s \boldsymbol{u}_s \; dS \tag{3a}$$

$$\boldsymbol{\Omega} = -\frac{3}{8\pi a^3} \int_s \hat{\boldsymbol{n}} \times \boldsymbol{u}_s \; dS \tag{3b}$$

where dS is a differential element of the surface, and the domain of integration is over the entire surface of the particle S.

Equation (3) relates the slip velocity on the particle surface to the net motion of the particle. The slip velocity arises from the interaction between the solute molecule and the particle's surface. It is well-known that a solute gradient along the particle's surface induces an osmotic pressure gradient, generating a fluid flow within the Debye layer of the particle's surface. In the thin Debye layer limit,[5] this slip velocity is assumed to be located on the Janus particle surface and given by

$$\boldsymbol{u}_s = -b(\hat{\boldsymbol{n}}) \nabla_s C \big|_s \tag{4}$$

where C is the fuel concentration field, $\nabla_s = (\mathbb{I} - \hat{\boldsymbol{n}}\hat{\boldsymbol{n}}) \cdot \nabla$ the tangential projection of the surface gradient operator, and $\hat{\boldsymbol{n}}$ the normal unit vector on the Janus particle surface directed into the bulk solution. The phoretic mobility $b(\hat{\boldsymbol{n}})$ can be either positive or negative and is determined by the details of the molecular interaction between the Janus particle and the solute particles.[5,69] We assume the particle's phoretic mobility is constant in a given surface region and denote the particle's absorbing and emitting sides as b_a and b_e, respectively. A central quantity in this study is the ratio of the phoretic mobilities of the two regions, which we call the phoretic mobility ratio and denote by $\beta = b_a/b_e$.

We treat the solute flux as being purely diffusive such that the fuel concentration field evolves according to the continuity equation $\partial_t C = D\nabla^2 C + \alpha\, \delta(\boldsymbol{r})$ where D is the diffusivity of the solute and α is the strength of the singularity, which can be positive or negative. Furthermore, it is reasonable to assume the fuel concentration field relaxes rapidly with respect to the particle's motion such that we can neglect its time dependence and assume $\partial C/\partial t = 0$. Under these conditions, the fuel concentration C is given by Laplace's equation with a point singularity at the origin

$$D\nabla^2(C - C_\infty) + \alpha\ \delta(\boldsymbol{r}) = 0\,. \tag{5}$$

The boundary condition on the surface of the Janus particle is given by

$$-D\hat{\boldsymbol{n}} \cdot \nabla C(\boldsymbol{r}) = Q_e H(\hat{\boldsymbol{n}} \cdot \hat{\boldsymbol{d}} + \chi) - Q_a \left[1 - H(\hat{\boldsymbol{n}} \cdot \hat{\boldsymbol{d}} + \chi)\right] \tag{6}$$

where $H(x)$ is the Heaviside function. The boundary condition for the fuel concentration is assumed to be constant at infinity and denoted by C_∞.

To summarize our workflow for obtaining the particle's trajectory, we first solve Eq. (5) with the appropriate boundary conditions to determine the concentration gradient along the surface of the Janus particle. Once the gradient of the concentration field is known, we can compute the slip velocity along the surface of the particle via Eq. (4), which in turn furnishes the translation and angular velocities via Eq. (3). The final step is to obtain the particle's trajectory by integrating Eq. (1) with the known translational and angular velocities.

Results

A central outcome of this work is an analytical solution for the translational and rotational velocity of the Janus particle as a function of the ratio of the phoretic mobilities $\beta = b_a/b_e$, the intrinsic velocity of the particle $U_0 = Q_e b_e/(2D)$, and the effective strength of the singularity

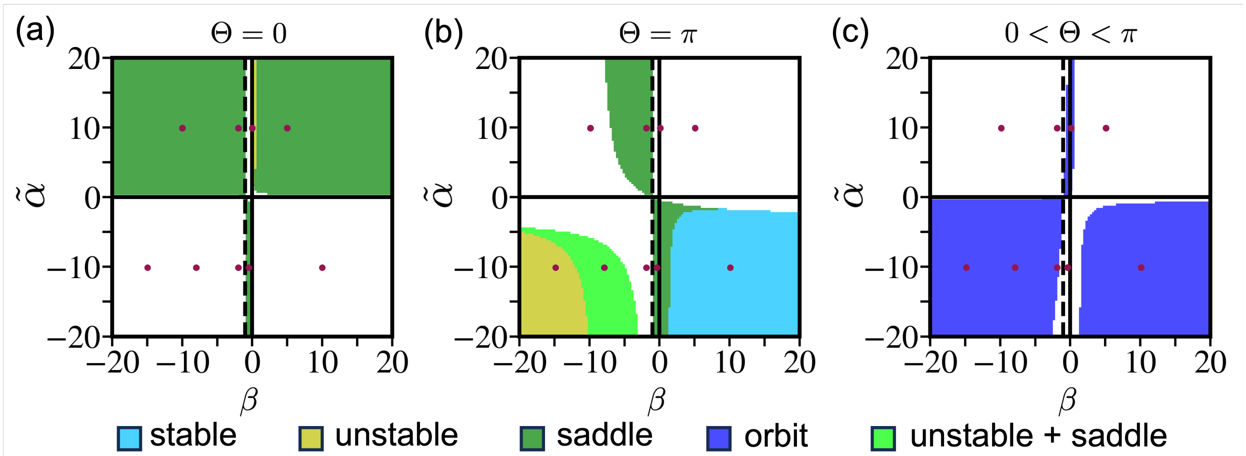

Figure 2: Classification of the different types of fixed points that can arise as a function of the ratio of the phoretic mobilities β and singularity strength $\tilde{\alpha}$ for a phoretic Janus particle with $\chi = 0$ and $U_0 = 1$. For clarity, the fixed point state diagrams are organized based on the particle's orientation: (a) $\Theta = 0$, (b) $\Theta = \pi$, and (c) $0 < \Theta < \pi$. The purple points correspond to representative values in the $\tilde{\alpha}\beta$-phase space where the $R\Theta$-phase portrait and real-space trajectories are given in Fig. 3 and Fig. 4. The dashed line at $\beta = -1$ corresponds to where the velocity vanishes for an isolated Janus particle, demarcating whether a particle will propel along or opposite its orientation vector.

$\tilde{\alpha} = \alpha/(4\pi a^2 Q_e)$. We present the final result here for brevity, but a detailed derivation is available in the Supporting Information.[70] The radial, tangential, and angular velocities of the particle are given by

$$\frac{U_R}{U_0} = \Gamma[\chi, \beta] \cos\Theta - \tilde{\alpha}\left(2\frac{a^2}{R^2} - (1-\beta)M[\chi, R, \Theta]\right) \tag{7a}$$

$$\frac{U_\varphi}{U_0} = \sin\Theta\Big(\Gamma[\chi, \beta] - \tilde{\alpha}(1-\beta)N[\chi, R, \Theta]\Big) \tag{7b}$$

$$\frac{\Omega_z}{U_0/a} = -\frac{3}{2}\tilde{\alpha}(1-\beta)\sin\Theta\ \omega[\chi, R, \Theta] \tag{7c}$$

where $\Gamma[\chi, \beta] = 1 + \chi - (1-\beta)B[\chi]$ is a positive dimensionless parameter that modulates the particle's intrinsic velocity. The functional form of $B[\chi]$ is given in the Supporting Information[70] along with a plot illustrating its dependence on the Janus balance χ, which shows $B[\chi] = 0$ for $\chi = -1$ and $\chi = 1$, and obtains its maximum value of $B[\chi] = 0.5$ for $\chi = 0$.

The dimensionless parameters $M[\chi, R, \Theta]$, $N[\chi, R, \Theta]$, and $\omega[\chi, R, \Theta]$ are given as infinite series whose explicit form are in the Supporting Information.[70] Each dimensionless parameter is a positive monotonically decreasing function of R where the leading order term decays as $1/R^2$. For the equal Janus balance case $\chi = 0$, we show the radial dependence of these dimensionless parameters for different values of the orientation Θ in the Supporting Information.[70] The analytical solution for the velocities and the resulting trajectories are in excellent agreement with Boundary Element Method simulations (see Supporting Information[70]).

The particle's motion is confined to the plane containing its orientation vector $\hat{\boldsymbol{d}}$ and radial vector $\hat{\boldsymbol{R}}$ and the only nonzero component of the angular velocity is normal to this plane. The first terms of Eqs. (7a) and (7b) correspond to the translational velocity of an isolated phoretic Janus particle. The second terms in each expression correspond to the velocity induced by the radial gradient generated by the singularity. Far from the singularity (i.e., $R \to \infty$), these terms vanish, and Eq. (7) reduces to that of a phoretic Janus particle in free space. The angular velocity of the particle Ω_z [Eq. (7c)] is due exclusively to the presence of the singularity and is strictly zero when $\beta = 1$. For other values of β, the presence of the singularity can induce particle rotation.

As the motion of the Janus particle is deterministic and completely specified by its initial position and orientation, we find that unless there exists an orbiting trajectory or a stationary point where the velocities vanish, the particle will either eventually collide with the singularity or move off to infinity. Thus, a natural scheme for classifying the dynamical behavior is identifying when fixed points occur as a function of the singularity strength $\tilde{\alpha}$ and the particle's surface properties.

The analytical solution for the particle's velocity facilitates determining the location of fixed points and the particle's trajectory for any $\tilde{\alpha}$, β, χ, or U_0. However, for simplicity, we restrict our discussion to a particle with equal Janus balance $\chi = 0$ and $U_0 = 1$. The equal Janus balance case is representative of many experimental systems and qualitatively illustrates the main features of the dynamics, including the emergence of fixed points. The

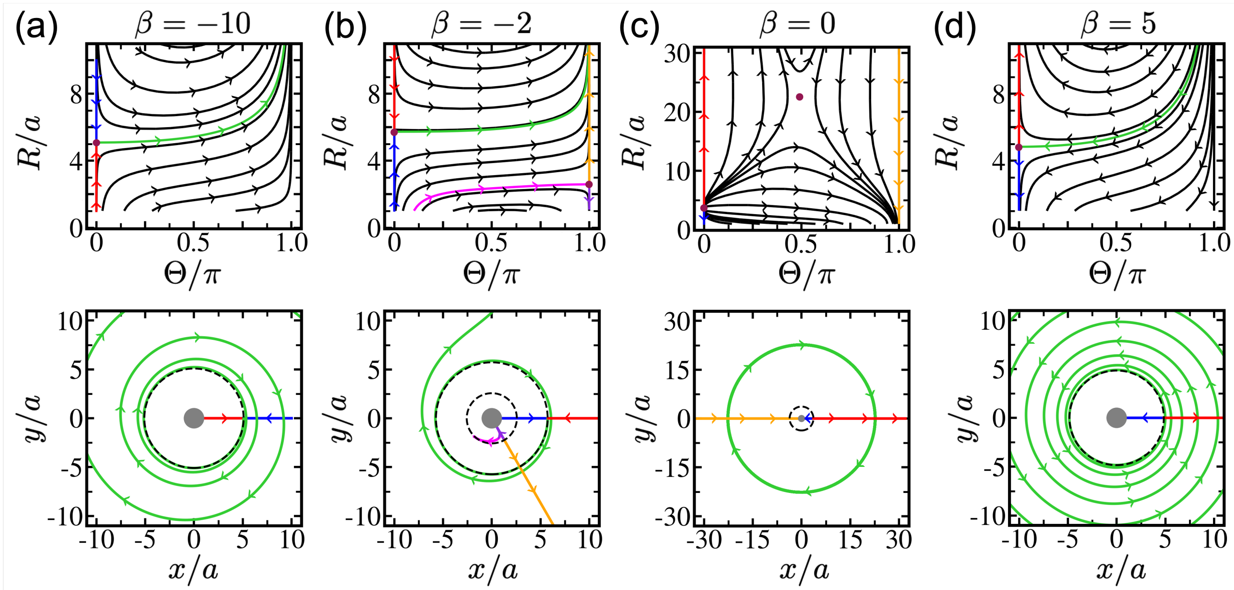

Figure 3: Dynamics near a chemical source: Phase portrait (top) and real-space trajectories (bottom) for phoretic Janus particles with different ratios of the phoretic mobilities β in the presence of a point source $\tilde{\alpha} = 10$. For each plot, particles have an equal Janus balance $\chi = 0$, and the intrinsic velocity of the particle is $U_0 = 1$. The fixed points are shown as purple circles, and the $R\Theta$-phase space trajectories and real space trajectories are color-coded accordingly. Videos of real-space trajectories are provided in the Supporting Information.[70]

most critical parameters impacting a particle's dynamics are the phoretic mobility ratio β and the singularity strength $\tilde{\alpha}$. The singularity strength $\tilde{\alpha}$ is the only direct and easily controllable parameter of the problem, whereas the material properties of the Janus particle will determine the phoretic mobility ratio β. Hence, we investigate the occurrence of fixed points as a function of $\tilde{\alpha}$ and β, which we refer to as the $\tilde{\alpha}\beta$-phase space.

For each point in the $\tilde{\alpha}\beta$-phase space, we conducted an exhaustive search as a function of R and Θ to identify where the different components of the velocities vanish. In our fixed point classification scheme, we recognize a *trapped* or stationary state when U_R, U_φ and $d\Theta/dt$ vanish and an orbiting state when only U_R and $d\Theta/dt$ vanish with U_φ remaining finite. As shown in Fig. 2, by analyzing the eigenvalues of the Jacobian about a fixed point,[71] we identify three types of stationary states: stable, unstable, and saddle, as well as an orbiting state. Stable fixed points are stationary states where any small perturbation in R or Θ will result in the particle returning to the initial fixed point. Unstable fixed points

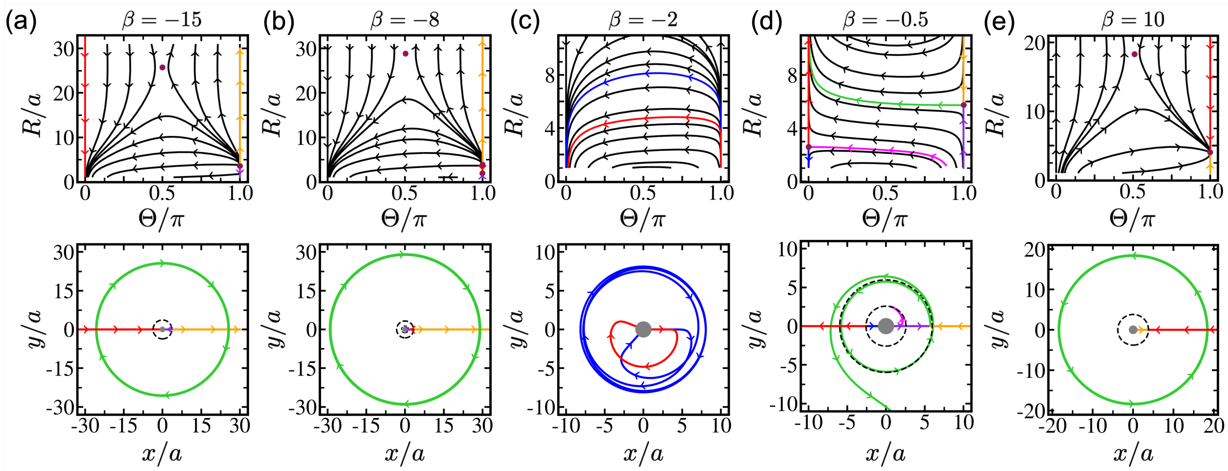

Figure 4: Dynamics near a chemical sink: Phase portrait (top) and real-space trajectories (bottom) for phoretic Janus particles with different ratios of the phoretic mobilities β in the presence of a point sink $\alpha = -10$. The other parameters are the same as Fig. 3, i.e., $\chi = 0$ and $U_0 = 1$. Videos of real-space trajectories are provided in the Supporting Information.[70]

exhibit opposite behavior where any small perturbation in R or Θ will lead to the particle moving away from the fixed point. Saddle points are of a mixed character where it is stable for small perturbations in R and unstable for perturbations in Θ, or vice versa. The defining feature of an orbiting state is that the particle's trajectory executes a closed circular path about the singularity. We use a similar classification for the stability of orbiting states.

For clarity, the fixed point state diagram is divided based on the particle's orientation where Fig. 2(a,b,c) corresponds to $\Theta = 0$, $\Theta = \pi$ and $0 < \Theta < \pi$, respectively. For the values of $\tilde{\alpha}$ and β located in the white regions of Fig. 2, no fixed point exists for any position and orientation. An important landmark in the $\tilde{\alpha}\beta$-phase space is the value of β, where the particle's intrinsic velocity vanishes. From Eq. (7), the intrinsic velocity vanishes for values of β that satisfy $1 + \chi - (1 - \beta)B[\chi] = 0$. In the equal Janus balance case, $B[\chi = 0] = 0.5$, and thus the intrinsic velocity is zero for $\beta = -1$ (dashed line in Fig. 2), For this value of β, any particle motion is due solely to the presence of the radial gradient. For values of $\beta < -1$, an isolated particle with $U_0 > 0$ moves with the absorbing side of the particle in front (i.e., along the $-\hat{\boldsymbol{d}}$ direction in Fig. 1), and for $\beta > -1$, the particle moves with the emitting side of the particle in front.

Figure 2(a) highlights the region in the $\tilde{\alpha}\beta$-phase space where fixed points exist for $\Theta = 0$. In this case, the orientation vector $\hat{\boldsymbol{d}}$ is parallel to the radial vector $\boldsymbol{R}$ (i.e., the emitting side of the particle is furthest from the source) and from Eq. (7), $U_\varphi = \Omega_z = 0$. Most fixed points are saddle points and occur for a point source $\tilde{\alpha} > 0$. However, there is a narrow region between $-1 < \beta < 0$ where we find saddle points for a point sink. Additionally, there is a narrow region $0 \leq \beta \leq 1$ where it is possible to have an unstable fixed point. A wider variety of fixed points occur for $\Theta = \pi$, where the emitting side of the particle is closest to the source [see Fig. 2(b)]. As the phoretic mobility ratio increases, there are regions in the $\tilde{\alpha}\beta$-phase space with an unstable stationary point, both an unstable point and saddle point, a saddle point, and a stable point. When a particle is in the presence of a point source, only saddle points are observed for $\Theta = \pi$, and the unstable and stable fixed points arise in the presence of a point sink. For intermediate orientations $0 < \Theta < \pi$, we find all fixed points are orbiting states and are more prevalent when the particle is in the presence of a point source [see Fig. 2(c)].

As a function of the source strength $\tilde{\alpha}$, the occurrence and disappearance of a particular combination of fixed points can be used to deduce the approximate range of a particle's phoretic mobility ratio β. The physical explanation for the emergence of a fixed point is a particle adopts an orientation and distance from the source such that the relevant components of its intrinsic velocity are equal and opposite to the velocities induced by the presence of the singularity, resulting in those components of the velocity vanishing. In general, fixed points are a robust feature of a phoretic Janus particle in a radially symmetric gradient. Similar behavior was observed for particles with different Janus balances χ.

We now survey in more detail the different dynamical behaviors that arise in the $\tilde{\alpha}\beta$-phase space by examining the $R\Theta$-phase portrait and the corresponding real space trajectories for selected values of $\tilde{\alpha}$ and β. For a known source strength $\tilde{\alpha}$, the location and type of the fixed point and, more generally, the $R\Theta$-phase portrait serve as a fingerprint for the particle's surface properties. In Fig. 3, we consider the case of a point source and choose a representative source strength of $\tilde{\alpha} = 10$ and explore various values of β, which span the different regions outlined in Fig. 2. In the Supporting Information,[70] we include figures that illustrate how the location of the fixed points and orbits change as a function of the strength of the singularity $\tilde{\alpha}$. The general trend is that the location of the fixed point moves further away from the singularity as its strength increases. Similarly, the orbit radius increases for orbiting states as the singularity strength increases, and the particle's orientation asymptotically approaches $\Theta \to \pi/2$. These trends agree with our previously mentioned physical interpretation, whereas the strength of the singularity increases, so does the contribution to the particles' velocity from the presence of the singularity. Thus, for a given intrinsic velocity of the particle U_0, a fixed point or orbiting state will occur at a further distance from the singularity or its orientation closer to $\pi/2$ to cancel the increased contribution to the velocity from increasing the strength of the singularity.

In Fig. 3(a), we start with the most negative value of the phoretic mobility ratio, $\beta = -10$, where there is a single saddle point at $\Theta/\pi = 0$ and $R/a \approx 5.1$. The saddle point is stable in R, as shown by the red and blue trajectories, where any displacement will lead to the particle moving back toward the fixed point and unstable for Θ, where any slight variation from $\Theta/\pi = 0$ will lead the particle to move toward infinity in a clockwise spiraling trajectory (green trajectory). As the phoretic mobility increases, we enter a region where two saddle points emerge in the $R\Theta$-phase portrait. For example, for $\beta = -2$, there are saddle points for $\Theta/\pi = 0$ and $\Theta/\pi = \pi$ at a distance of $R/a \approx 5.7$ and $R/a \approx 2.5$, respectively [see Fig. 3(b)]. The further saddle point is similar to that identified for $\beta = -10$ and is stable in R. However, the saddle point that emerges closer to the source exhibits the opposite behavior, where it is stable for changes in Θ.

As β transitions from negative to positive values, in addition to the saddle point for $\Theta = 0$, a saddle orbiting state emerges at $\Theta/\pi \approx 0.5$ and $R/a \approx 22$ [see Fig 3(c) for the $R\Theta$-phase portrait and real space trajectories for $\beta = 0$]. Particles with this initial orientation and position will execute a clockwise orbit about the source (green trajectory). For $\beta \gtrsim 1$, we enter a region with only a single saddle point. The phase portrait resembles the case for large negative values of the ratio of the phoretic mobilities (i.e., $\beta < -10$). However, the direction of the trajectories is reversed in the $R\Theta$-phase portrait as shown in Fig. 3(d) for $\beta = 5$. The saddle point occurs for $\Theta/\pi = 0$ and $R/a \approx 4.8$ and is unstable in R and stable for Θ. The green trajectory in Fig 3(d) is associated with the saddle point, and the particle undergoes a counterclockwise spiraling motion until it reaches the saddle point.

Figure 4 illustrates the different dynamical behaviors that can arise for a point sink. We select a representative sink strength of $\tilde{\alpha} = -10$ to demonstrate the variation in the $R\Theta$-phase portrait as a function of the phoretic mobility ratio β. In Fig. 4(a), we begin with the most negative value of the phoretic mobility ratio $\beta = -15$ where there are two fixed points: an unstable point for $\Theta/\pi = 1.0$ at $R/a \approx 3.5$, and an orbiting state for $\Theta/\pi \approx 0.51$ and $R/a \approx 25.6$. This point is within one of the few regions in the $\tilde{\alpha}\beta$-phase space where we observe an unstable fixed point. The other is a narrow region for $\beta \approx 0.2$ and $\tilde{\alpha} > 0$. Interestingly, unstable fixed points will become stable under the reversal of the intrinsic velocity U_0. It is important to note the sign of U_0 does not alter the location of the fixed points in the $\tilde{\alpha}\beta$-phase space. From Eq. 7, reversing the sign of U_0 will only lead to a reversal of the velocities. Thus, the $R\Theta$-phase portraits given in Fig. 3 and Fig. 4 for $U_0 = 1$ will have the same topology as $U_0 = -1$. However, the arrows indicating the direction of motion are reversed. Thus, a stable point for $U_0 > 0$ will become an unstable point for $U_0 < 0$. Similarly, a saddle point stable in R for $U_0 > 0$ will be unstable in R for $U_0 < 0$.

As the phoretic mobility ratio increases, the next region has three fixed points: an unstable stationary state, a saddle point, and an orbiting state. A representative example is shown in Fig. 4(b) for $\beta = -8$. The emergent saddle point occurs for $\Theta/\pi = 1.0$, is close to the singularity at $R/a \approx 1.4$, and is stable for variations in R but not Θ. The unstable point occurs at $R/a \approx 3.8$ also for $\Theta/\pi = 1.0$. The next region represented by $\beta = -2$ [Fig. 4(c)] contains no fixed points, and the particle eventually collides with the singularity unless the initial orientation is $\Theta/\pi = 1$ where it moves off to infinity. Interestingly, particles starting

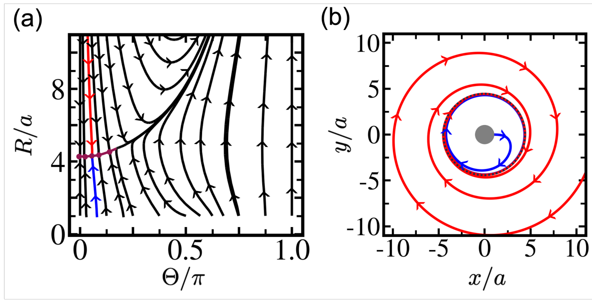

Figure 5: Infinite number of orbiting states: (a) $R\Theta$-phase portrait and (b) real-space trajectory in the region of the $\tilde{\alpha}\beta$-phase space where a continuous and infinite number of orbiting fixed points exists about the source. These plots correspond to the parameter values $\tilde{\alpha} = 10$, $\beta = 0.644$, $\chi = 0$ and $U_0 = -1$. Videos of the real-space trajectories of these orbiting states are provided in the Supporting Information.[70]

with their orientation closer to $\Theta/\pi = 1$ can undergo a trajectory that will wind several times about the singularity before being drawn toward the center (blue trajectory). In Fig. 4(d), we show the case of $\beta = -0.5$, where there exist two saddle points one located at $\Theta/\pi = 0$ and $\Theta/\pi = 1.0$ The phase portrait is similar to $\beta = -2$ and $\tilde{\alpha} = 10$ [see Fig. 3(b)], except for it being reflected about the line $\Theta/\pi = 0.5$.

In Fig. 4(e), we show the case of $\beta = 10$, which is representative of the only region of the $\tilde{\alpha}\beta$-phase space with a stable fixed point, which occurs for $\Theta/\pi = 1.0$ and has a distance of $R/a \approx 3.9$ from the singularity. A unique feature of this region of the $\tilde{\alpha}\beta$-phase space is the $R\Theta$-phase portrait shows an exclusion region between the location of the singularity and the fixed point. Any particle initially in the region will either migrate toward the fixed point or off to infinity. This behavior mirrors the movement pattern observed in a recent study of *P. aeruginosa* bacteria in response to a CO_2 point source, where the cells form an accumulation front at a distance from the source.[72] Stable fixed points of this character have potential applications in surface cleaning from bio-contaminants or preventing the accumulation of active particles near surfaces.

We conclude by highlighting a peculiar region of the $\tilde{\alpha}\beta$-phase space not categorized in Fig. 2, where we observed a continuum of orbiting states. A representative example of this behavior occurs for $U_0 = -1$, $\tilde{\alpha} = 10$ and $\beta \approx 0.64$, and the corresponding phase portrait and real space trajectories are given in Fig. 5. The magenta line in the $R\Theta$-phase portrait represents an infinite number of orbiting states that are stable with variations in R and neutrally stable for Θ. Thus, any small changes in Θ or R will lead to the particle finding a new orbit with a different radius. This behavior, where there was observed to be a continuum of orbiting states, only occurs in a very small region of the $\tilde{\alpha}\beta$-phase space and will be further characterized in future work.

Conclusion

In this study, we quantified the dynamics of a phoretic Janus particle in a radially symmetric gradient generated by a point source or sink of the fuel driving self-propulsion. We derived an analytical expression for the phoretic Janus particle's velocity and found that its motion is highly sensitive to its surface properties and can exhibit various dynamical behaviors. In addition to positive and negative chemotaxis, we identify system parameters that give rise to circular orbits and trapped stationary states. We show that both types of fixed points are a robust feature of the $\tilde{\alpha}\beta$-phase space. The sensitivity of the location of the fixed points and, more generally, the topology of the $R\Theta$-phase portrait that characterizes their trajectories suggests a method for quantifying the surface properties of phoretic Janus particles.

In addition, circular orbits and trapped stationary states offer a mechanism for pumping fluid and mixing at the microscale, particularly the stable stationary states, which are resistant to small fluctuations usually present in an experimental setting. Even when a particle is trapped in a stationary or orbiting state, its surface is still chemically active and will pump fluid across its surface. Our results demonstrate how to tune the location of a trapped or orbiting state via the strength of the source and the particle's phoretic mobility ratio. This ability to localize particles at a particular distance from the singularity suggests the possibility of achieving controlled fluid mixing at a desired rate, which is challenging at the microscale.

Future research related to this work includes investigating the role of chemical solute convection and the effect of Brownian motion on the dynamics in a radial chemical gradient. In addition, to better align the model to many experimental systems, we are currently investigating the role of a confining boundary, as many phoretic Janus particles are confined to move at a two-dimensional surface.

Supporting Information Available

See Supporting Information at [URL] for complete derivation of the velocity of phoretic Janus particle, plot illustrating the radial dependence of dimensionless parameters in solution of Janus particles velocity, plot characterizing the location of fixed points as a function of the strength of the singularity, and movies illustrating the real space trajectories for different system parameters.

References

(1) Xu, L.; Mou, F.; Gong, H.; Luo, M.; Guan, J. Light-Driven Micro/Nanomotors: From Fundamentals to Applications. *Chem. Soc. Rev.* **2017**, *46*, 6905–6926.

(2) Venugopalan, P. L.; Esteban-Fernández de Ávila, B.; Pal, M.; Ghosh, A.; Wang, J. Fantastic Voyage of Nanomotors Into the Cell. *ACS Nano* **2020**, *14*, 9423–9439.

(3) Zhang, H.; Li, Z.; Gao, C.; Fan, X.; Pang, Y.; Li, T.; Wu, Z.; Xie, H.; He, Q. Dual-Responsive Biohybrid Neutrobots for Active Target Delivery. *Sci. Robot.* **2021**, *6*, eaaz9519.

(4) Zhang, X.; Fu, Q.; Duan, H.; Song, J.; Yang, H. Janus Nanoparticles: From Fabrication to (Bio) Applications. *ACS Nano* **2021**, *15*, 6147–6191.

(5) Anderson, J. L. Colloid Transport by Interfacial Forces. *Annu. Rev. Fluid Mech.* **1989**, *21*, 61–99.

(6) Prieve, D. C.; Anderson, J. L.; Ebel, J. P.; Lowell, M. E. Motion of a Particle Generated by Chemical Gradients. Part 2. Electrolytes. *J. Fluid Mech.* **1984**, *148*, 247–269.

(7) Safdar, M.; Khan, S. U.; Jänis, J. Progress Toward Catalytic Micro-and Nanomotors for Biomedical and Environmental Applications. *Adv. Mater.* **2018**, *30*, 1703660.

(8) Paxton, W. F.; Kistler, K. C.; Olmeda, C. C.; Sen, A.; St. Angelo, S. K.; Cao, Y.; Mallouk, T. E.; Lammert, P. E.; Crespi, V. H. Catalytic Nanomotors: Autonomous Movement of Striped Nanorods. *J. Am. Chem. Soc.* **2004**, *126*, 13424–13431.

(9) Theurkauff, I.; Cottin-Bizonne, C.; Palacci, J.; Ybert, C.; Bocquet, L. Dynamic Clustering in Active Colloidal Suspensions With Chemical Signaling. *Phys. Rev. Lett.* **2012**, *108*, 268303.

(10) Solovev, A. A.; Mei, Y.; Bermúdez Ureña, E.; Huang, G.; Schmidt, O. G. Catalytic Microtubular Jet Engines Self-Propelled by Accumulated Gas Bubbles. *Small* **2009**, *5*, 1688–1692.

(11) Solovev, A. A.; Smith, E. J.; Bof'Bufon, C. C.; Sanchez, S.; Schmidt, O. G. Light-Controlled Propulsion of Catalytic Microengines. *Angew. Chem.* **2011**, *50*, 10875.

(12) Gao, W.; Sattayasamitsathit, S.; Orozco, J.; Wang, J. Highly Efficient Catalytic Microengines: Template Electrosynthesis of Polyaniline/Platinum Microtubes. *J. Am. Chem. Soc.* **2011**, *133*, 11862–11864.

(13) Sanchez, S.; Ananth, A. N.; Fomin, V. M.; Viehrig, M.; Schmidt, O. G. Superfast Motion of Catalytic Microjet Engines at Physiological Temperature. *J. Am. Chem. Soc.* **2011**, *133*, 14860–14863.

(14) Lee, T.-C.; Alarcon-Correa, M.; Miksch, C.; Hahn, K.; Gibbs, J. G.; Fischer, P. Self-Propelling Nanomotors in the Presence of Strong Brownian Forces. *Nano Lett.* **2014**, *14*, 2407–2412.

(15) Martín, A.; Jurado-Sánchez, B.; Escarpa, A.; Wang, J. Template Electrosynthesis of High-Performance Graphene Microengines. *Small* **2015**, *11*, 3568–3574.

(16) Okmen Altas, B.; Goktas, C.; Topcu, G.; Aydogan, N. Multi-Stimuli-Responsive Tadpole-Like Polymer/Lipid Janus Microrobots for Advanced Smart Material Applications. *ACS Appl. Mater. Interfaces.* **2024**,

(17) Maiti, S.; Shklyaev, O. E.; Balazs, A. C.; Sen, A. Self-Organization of Fluids in a Multienzymatic Pump System. *Langmuir* **2019**, *35*, 3724–3732.

(18) Patiño, T.; Arqué, X.; Mestre, R.; Palacios, L.; Sánchez, S. Fundamental Aspects of Enzyme-Powered Micro- And Nanoswimmers. *Acc. Chem. Res.* **2018**, *51*, 2662–2671.

(19) Lu, C.; Liu, X.; Li, Y.; Yu, F.; Tang, L.; Hu, Y.; Ying, Y. Multifunctional Janus Hematite–Silica Nanoparticles: Mimicking Peroxidase-Like Activity and Sensitive Colorimetric Detection of Glucose. *ACS Appl. Mater. Interfaces* **2015**, *7*, 15395–15402.

(20) Tan, K. X.; Danquah, M. K.; Jeevanandam, J.; Barhoum, A. Development of Janus Particles as Potential Drug Delivery Systems for Diabetes Treatment and Antimicrobial Applications. *Pharmaceutics* **2023**, *15*, 423.

(21) Vilela, D.; Parmar, J.; Zeng, Y.; Zhao, Y.; Sánchez, S. Graphene-Based Microbots for Toxic Heavy Metal Removal and Recovery From Water. *Nano Lett.* **2016**, *16*, 2860–2866.

(22) Villa, K.; Parmar, J.; Vilela, D.; Sánchez, S. Metal-Oxide-Based Microjets for the Simultaneous Removal of Organic Pollutants and Heavy Metals. *ACS Appl. Mater. Interfaces* **2018**, *10*, 20478–20486.

(23) Fu, T.; Zhang, B.; Gao, X.; Cui, S.; Guan, C.-Y.; Zhang, Y.; Zhang, B.; Peng, Y. Recent Progresses, Challenges, and Opportunities of Carbon-Based Materials Applied in Heavy Metal Polluted Soil Remediation. *Sci. Total Environ.* **2023**, *856*, 158810.

(24) Soler, L.; Magdanz, V.; Fomin, V. M.; Sanchez, S.; Schmidt, O. G. Self-Propelled Micromotors for Cleaning Polluted Water. *ACS Nano* **2013**, *7*, 9611–9620.

(25) Wani, O. M.; Safdar, M.; Kinnunen, N.; Jänis, J. Dual Effect of Manganese Oxide Micromotors: Catalytic Degradation and Adsorptive Bubble Separation of Organic Pollutants. *Chem. Eur. J.* **2016**, *22*, 1244–1247.

(26) Mushtaq, F.; Asani, A.; Hoop, M.; Chen, X.-Z.; Ahmed, D.; Nelson, B. J.; Pané, S. Highly Efficient Coaxial TiO2-PtPd Tubular Nanomachines for Photocatalytic Water Purification With Multiple Locomotion Strategies. *Adv. Funct. Mater.* **2016**, *26*, 6995–7002.

(27) Zhang, Q.; Dong, R.; Wu, Y.; Gao, W.; He, Z.; Ren, B. Light-Driven Au-Wo3@c Janus Micromotors for Rapid Photodegradation of Dye Pollutants. *ACS Appl. Mater. Interfaces* **2017**, *9*, 4674–4683.

(28) Wang, L.; Kaeppler, A.; Fischer, D.; Simmchen, J. Photocatalytic TiO2 Micromotors for Removal of Microplastics and Suspended Matter. *ACS Appl. Mater. Interfaces* **2019**, *11*, 32937–32944.

(29) Beladi-Mousavi, S. M.; Hermanova, S.; Ying, Y.; Plutnar, J.; Pumera, M. A Maze in Plastic Wastes: Autonomous Motile Photocatalytic Microrobots Against Microplastics. *ACS Appl. Mater. Interfaces* **2021**, *13*, 25102–25110.

(30) Ghosh, A.; Xu, W.; Gupta, N.; Gracias, D. H. Active Matter Therapeutics. *Nano Today* **2020**, *31*.

(31) Guix, M.; Meyer, A. K.; Koch, B.; Schmidt, O. G. Carbonate-based Janus micromotors moving in ultra-light acidic environment generated by HeLa cells in situ. *Sci. Rep.* **2016**, *6*, 21701.

(32) Mallory, S. A.; Valeriani, C.; Cacciuto, A. An Active Approach to Colloidal Self-Assembly. *Annu. Rev. Phys. Chem.* **2018**, *69*, 59–79.

(33) Mallory, S. A.; Cacciuto, A. Activity-Enhanced Self-Assembly of a Colloidal Kagome Lattice. *J. Am. Chem. Soc.* **2019**, *141*, 2500–2507.

(34) Szakasits, M. E.; Zhang, W.; Solomon, M. J. Dynamics of Fractal Cluster Gels With Embedded Active Colloids. *Phys. Rev. Lett.* **2017**, *119*, 058001.

(35) Szakasits, M. E.; Saud, K. T.; Mao, X.; Solomon, M. J. Rheological implications of embedded active matter in colloidal gels. *Soft Matter* **2019**, *15*, 8012–8021.

(36) Omar, A. K.; Wu, Y.; Wang, Z.-G.; Brady, J. F. Swimming to Stability: Structural and Dynamical Control via Active Doping. *ACS Nano* **2019**, *13*, 560–572.

(37) Mallory, S. A.; Bowers, M. L.; Cacciuto, A. Universal Reshaping of Arrested Colloidal Gels via Active Doping. *J. Chem. Phys.* **2020**, *153*, 084901.

(38) Maggi, C.; Simmchen, J.; Saglimbeni, F.; Katuri, J.; Dipalo, M.; De Angelis, F.; Sanchez, S.; Di Leonardo, R. Self-Assembly of Micromachining Systems Powered by Janus Micromotors. *Small* **2016**, *12*, 446–451.

(39) Soto, F.; Karshalev, E.; Zhang, F.; Esteban Fernandez de Avila, B.; Nourhani, A.; Wang, J. Smart Materials for Microrobots. *Chem. Rev.* **2022**, *122*, 5365–5403.

(40) Liu, T.; Xie, L.; Price, C.-A. H.; Liu, J.; He, Q.; Kong, B. Controlled propulsion of micro/nanomotors: operational mechanisms, motion manipulation and potential biomedical applications. *Chem. Soc. Rev.* **2022**, *51*, 10083–10119.

(41) Yu, T.; Athanassiadis, A. G.; Popescu, M. N.; Chikkadi, V.; Güth, A.; Singh, D. P.; Qiu, T.; Fischer, P. Microchannels With Self-Pumping Walls. *ACS Nano* **2020**, *14*, 13673–13680.

(42) Uspal, W.; Popescu, M. N.; Dietrich, S.; Tasinkevych, M. Self-Propulsion of a Catalytically Active Particle Near a Planar Wall: From Reflection to Sliding and Hovering. *Soft Matter* **2015**, *11*, 434–438.

(43) Bayati, P.; Popescu, M. N.; Uspal, W. E.; Dietrich, S.; Najafi, A. Dynamics Near Planar Walls for Various Model Self-Phoretic Particles. *Soft matter* **2019**, *15*, 5644–5672.

(44) Das, S.; Garg, A.; Campbell, A. I.; Howse, J.; Sen, A.; Velegol, D.; Golestanian, R.; Ebbens, S. J. Boundaries Can Steer Active Janus Spheres. *Nat. Commun.* **2015**, *6*, 8999.

(45) Wang, X.; In, M.; Blanc, C.; Nobili, M.; Stocco, A. Enhanced Active Motion of Janus Colloids at the Water Surface. *Soft Matter* **2015**, *11*, 7376–7384.

(46) Simmchen, J.; Katuri, J.; Uspal, W. E.; Popescu, M. N.; Tasinkevych, M.; Sánchez, S. Topographical Pathways Guide Chemical Microswimmers. *Nat. Commun.* **2016**, *7*, 1–9.

(47) Liu, C.; Zhou, C.; Wang, W.; Zhang, H. Bimetallic Microswimmers Speed Up in Confining Channels. *Phys. Rev. Lett.* **2016**, *117*, 198001.

(48) Wang, X.; In, M.; Blanc, C.; Wurger, A.; Nobili, M.; Stocco, A. Janus Colloids Actively Rotating on the Surface of Water. *Langmuir* **2017**, *33*, 13766–13773.

(49) Jalaal, M.; ten Hagen, B.; Diddens, C.; Lohse, D.; Marin, A. Interfacial Aggregation of Self-Propelled Janus Colloids in Sessile Droplets. *Phys. Rev. Fluids* **2022**, *7*, 110514.

(50) Yu, H.; Kopach, A.; Misko, V. R.; Vasylenko, A. A.; Makarov, D.; Marchesoni, F.; Nori, F.; Baraban, L.; Cuniberti, G. Confined Catalytic Janus Swimmers in a Crowded

Channel: Geometry-Driven Rectification Transients and Directional Locking. *Small* **2016**, *12*, 5882–5890.

(51) Jiang, H.-R.; Yoshinaga, N.; Sano, M. Active Motion of a Janus Particle by Self-Thermophoresis in a Defocused Laser Beam. *Phys. Rev. Lett.* **2010**, *105*, 268302.

(52) Auschra, S.; Bregulla, A.; Kroy, K.; Cichos, F. Thermotaxis of Janus Particles. *Eur. Phys. J. E* **2021**, *44*, 90.

(53) Chen, X.; Chen, X.; Elsayed, M.; Edwards, H.; Liu, J.; Peng, Y.; Zhang, H.; Zhang, S.; Wang, W.; Wheeler, A. R. Steering Micromotors via Reprogrammable Optoelectronic Paths. *ACS Nano* **2023**, *17*, 5894–5904.

(54) Sharifi-Mood, N.; Mozaffari, A.; Córdova-Figueroa, U. M. Pair Interaction of Catalytically Active Colloids: From Assembly to Escape. *J. Fluid Mech.* **2016**, *798*, 910–954.

(55) Mallory, S.; Alarcon, F.; Cacciuto, A.; Valeriani, C. Self-Assembly of Active Amphiphilic Janus Particles. *New J. Phys.* **2017**, *19*, 125014.

(56) Liebchen, B.; Lowen, H. Synthetic Chemotaxis and Collective Behavior in Active Matter. *Acc. Chem. Res.* **2018**, *51*, 2982–2990.

(57) Stark, H. Artificial Chemotaxis of Self-Phoretic Active Colloids: Collective Behavior. *Acc. Chem. Res.* **2018**, *51*, 2681–2688.

(58) Stürmer, J.; Seyrich, M.; Stark, H. Chemotaxis in a Binary Mixture of Active and Passive Particles. *J. Chem. Phys.* **2019**, *150*.

(59) Che, S.; Zhang, J.; Mou, F.; Guo, X.; Kauffman, J. E.; Sen, A.; Guan, J. Light-Programmable Assemblies of Isotropic Micromotors. *Research* **2022**,

(60) Singh, K.; Raman, H.; Tripathi, S.; Sharma, H.; Choudhary, A.; Mangal, R. Pair Interactions of Self-Propelled SiO2-Pt Janus Colloids: Chemically Mediated Encounters. *Langmuir* **2024**,

(61) Saha, S.; Golestanian, R.; Ramaswamy, S. Clusters, Asters, and Collective Oscillations in Chemotactic Colloids. *Phys. Rev. E* **2014**, *89*, 062316.

(62) Popescu, M. N.; Uspal, W. E.; Bechinger, C.; Fischer, P. Chemotaxis of Active Janus Nanoparticles. *Nano Lett.* **2018**, *18*, 5345–5349.

(63) Vinze, P. M.; Choudhary, A.; Pushpavanam, S. Motion of an Active Particle in a Linear Concentration Gradient. *Phys. Fluids* **2021**, *33*, 032011.

(64) Xiao, Z.; Nsamela, A.; Garlan, B.; Simmchen, J. A Platform for Stop-Flow Gradient Generation to Investigate Chemotaxis. *Angew. Chem.* **2022**, *61*, e202117768.

(65) Moran, J. L.; Posner, J. D. Phoretic Self-Propulsion. *Annu. Rev. Fluid Mech.* **2017**, *49*, 511–540.

(66) Bayati, P.; Najafi, A. Dynamics of Two Interacting Active Janus Particles. *J. Chem. Phys.* **2016**, *144*, 134901.

(67) Happel, J.; Brenner, H. *Low Reynolds Number Hydrodynamics: With Special Applications to Particulate Media*; Springer, 2012.

(68) Lauga, E.; Powers, T. R. The Hydrodynamics of Swimming Microorganisms. *Rep. Prog. Phys.* **2009**, *72*, 096601.

(69) Derjaguin, B. V.; Sidorenkov, G.; Zubashchenko, E.; Kiseleva, E. Kinetic Phenomena in the Boundary Layers of Liquids 1. The Capillary Osmosis. *Prog. Surf. Sci.* **1993**, *43*, 138–152.

(70) See Supporting Information at [URL] for complete derivation of the velocity of phoretic Janus particle, plot illustrating the radial dependence of dimensionless parameters in solution of Janus particles velocity, plot characterizing the location of fixed points as a function of the strength of the singularity, and movies illustrating the real space trajectories for different system parameters.

(71) Chasnov, J. R. *Differential Equations for Engineers (Mathematics for Engineers)*; Independently published, 2022.

(72) Shim, S.; Khodaparast, S.; Lai, C.-Y.; Yan, J.; Ault, J. T.; Rallabandi, B.; Shardt, O.; Stone, H. A. CO2-Driven Diffusiophoresis for Maintaining a Bacteria-Free Surface. *Soft Matter* **2021**, *17*, 2568–2576.

TOC Graphic

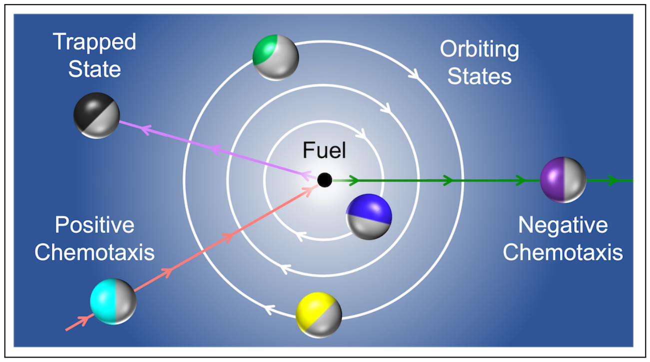
Trapped
State
Orbiting
States
Fuel
Positive
Chemotaxis
Negative
Chemotaxis

Supporting Information: Orbits, spirals, and trapped states: Dynamics of a phoretic Janus particle in a radial concentration gradient

Parvin Bayati† and Stewart A. Mallory*,†,‡

†*Department of Chemistry, The Pennsylvania State University, University Park, Pennsylvania, 16802, USA*

‡*Department of Chemical Engineering, The Pennsylvania State University, University Park, Pennsylvania, 16802, USA*

E-mail: sam7808@psu.edu

Analytical solution for phoretic Janus particle velocity

Due to the linearity of our governing equations [Eqs. (2) and (5) of the main text], we can apply the principle of superposition and decompose the solution for the total fuel solute concentration field into a sum of three elementary solutions, which we write as

$$C(\boldsymbol{r}) - C_\infty = C_{sin}(\boldsymbol{r}) + C_a(\boldsymbol{r}) + C_d(\boldsymbol{r})\,, \tag{S1}$$

where C_∞ is the constant bulk fuel concentration far from the particle and singularity. The concentration field C_{sin} corresponds to the problem of a point singularity of strength α

centered at the origin $\boldsymbol{r} = 0$, whose behavior is governed by

$$D\nabla^2 C_{sin} + \alpha\ \delta(\boldsymbol{r}) = 0\,, \tag{S2}$$

with far-field boundary condition $C_{sin}|_{r\to\infty} = 0$. The concentration field C_a corresponds to the problem of an isolated phoretic Janus particle with governing equation

$$\nabla^2 C_a = 0\,, \tag{S3}$$

with the boundary condition on the surface of the particle given by Eq. (6) of the main text and far-field boundary condition $C_a|_{r\to\infty} = 0$. The concentration field C_d also satisfies Laplace's equation, and is introduced to ensure the intrinsic activity of the Janus particle is not altered by the presence of the source. The requisite boundary condition along the surface of the particle is

$$\hat{\boldsymbol{n}} \cdot \nabla C_d|_s = -\hat{\boldsymbol{n}} \cdot \nabla C_{sin}|_s \tag{S4}$$

and the far-field boundary condition is $C_d|_{r\to\infty} = 0$.

The solutions for C_{sin} and C_a (see Ref.[1] for details) can be written in terms of Legendre polynomials $P_n[x]$ as

$$C_{sin}(\boldsymbol{r}_p) = C_0\tilde{\alpha}\frac{a}{|\boldsymbol{r}_p + \boldsymbol{R}|} = C_0\tilde{\alpha}\sum_{n\geq 0}(-1)^n\frac{a\, r_<^n}{r_>^{n+1}}P_n[\hat{\boldsymbol{R}}\cdot\hat{\boldsymbol{n}}] \tag{S5}$$

and

$$C_a(\boldsymbol{r}_p) = C_0\sum_{n\geq 1}\frac{K_n[\chi]}{(n+1)}\left(\frac{a}{r_p}\right)^{n+1}P_n[\hat{\boldsymbol{d}}\cdot\hat{\boldsymbol{n}}]\,, \tag{S6}$$

where $r_<$ and $r_>$ are chosen between r_p and R, $K_n[\chi] = (P_{n-1}[-\chi] - P_{n+1}[-\chi])/(1-\chi)$, $C_0 = aQ_e/D$, and $\tilde{\alpha} = \alpha/(4\pi a^2 Q_e)$. We define $\boldsymbol{r}_p$ as the position vector with respect to the coordinate frame centered on the particle such that $\boldsymbol{r} = \boldsymbol{r}_p + \boldsymbol{R}$ and $\boldsymbol{r}_p|_s = a\hat{\boldsymbol{n}}$. As $\boldsymbol{R}$ is constant for a given configuration, the gradient operator with respect to $\boldsymbol{r}_p$ and $\boldsymbol{r}$ are equal (i.e., $\nabla = \nabla_{\boldsymbol{r}} = \nabla_{\boldsymbol{r}_p}$). To obtain a solution for C_d, we first rewrite the boundary condition in Eq. (S4) in terms of Legendre polynomials as

$$\hat{\boldsymbol{n}} \cdot \nabla C_d|_s = \frac{C_0\, \tilde{\alpha}}{a} \sum_{n\geq 0} n \left(\frac{-a}{R}\right)^{n+1} P_n[\hat{\boldsymbol{R}} \cdot \hat{\boldsymbol{n}}]\,. \tag{S7}$$

Equation (S7) and the boundary condition at infinity suggests a solution for C_d can be written in terms of $\boldsymbol{r}_p$ and Legendre polynomials of the form

$$C_d(\boldsymbol{r}_p) = C_0 \tilde{\alpha} \sum_{n\geq 0} \frac{n(-1)^n}{n+1} \left(\frac{a^2}{R\, r_p}\right)^{n+1} P_n[\hat{\boldsymbol{R}} \cdot \hat{\boldsymbol{n}}]. \tag{S8}$$

The solution for the total concentration is the sum of C_a, C_{sin}, and C_d giving:

$$C(\boldsymbol{r}) = C_0 \sum_{n\geq 1} \frac{K_n[\chi]}{(n+1)} \left(\frac{a}{r_p}\right)^{n+1} P_n[\hat{\boldsymbol{d}} \cdot \hat{\boldsymbol{n}}] + C_0 \tilde{\alpha} \sum_{n\geq 0} (-1)^n \left(\frac{a\, r_<^n}{r_>^{n+1}} + \frac{n}{n+1} \left(\frac{a^2}{R\, r_p}\right)^{n+1}\right) P_n[\hat{\boldsymbol{R}} \cdot \hat{\boldsymbol{n}}]. \tag{S9}$$

Prior to calculating the slip velocity via Eq. (4) of the main text, we note that the phoretic mobility $b[\hat{\boldsymbol{n}}]$ for a spherical particle with bilateral symmetry can be expressed as

$$b[\hat{\boldsymbol{n}}]/b_e = \begin{cases} 1, & \hat{\boldsymbol{n}} \cdot \hat{\boldsymbol{d}} > -\chi \\ \beta, & \hat{\boldsymbol{n}} \cdot \hat{\boldsymbol{d}} < -\chi \\ \frac{1}{2}(1+\beta), & \hat{\boldsymbol{n}} \cdot \hat{\boldsymbol{d}} = -\chi \end{cases} = 1 - (1-\beta) H[-\hat{\boldsymbol{n}} \cdot \hat{\boldsymbol{d}} - \chi] \tag{S10}$$

where $H(x)$ is the Heaviside function. The Heaviside function in Eq. (S10) can be expanded in terms of Legendre polynomials as

$$H[-\hat{\boldsymbol{n}} \cdot \hat{\boldsymbol{d}} - \chi] = \frac{1}{2}(1-\chi) - \frac{1}{2}(1-\chi) \sum_{n\geq 1} K_n[\chi] P_n[\hat{\boldsymbol{n}} \cdot \hat{\boldsymbol{d}}], \tag{S11}$$

Then, noting that $\boldsymbol{r}_p = \boldsymbol{r} - \boldsymbol{R}$ and $\nabla = \nabla_{\boldsymbol{r}} = \nabla_{\boldsymbol{r_p}}$, we have

$$\nabla(\hat{\boldsymbol{n}} \cdot \hat{\boldsymbol{d}}) = (\hat{\boldsymbol{d}} \cdot \nabla)\hat{\boldsymbol{n}} = (\hat{\boldsymbol{d}} \cdot \nabla_{\boldsymbol{r_p}})\hat{\boldsymbol{n}} = \hat{\boldsymbol{d}} \cdot \left(\mathbb{I} - \hat{\boldsymbol{n}}\hat{\boldsymbol{n}}\right) \tag{S12}$$

and a similar relation can be derived for $\nabla(\hat{\boldsymbol{n}} \cdot \hat{\boldsymbol{R}})$. Using these relations and the concentration field given by Eq. (S9), the slip velocity can be expressed as

$$\boldsymbol{u}_s = -2U_0 \frac{b[\hat{\boldsymbol{n}}]}{b_e} \sum_{n\geq 1} \frac{1}{n+1} \left(K_n[\chi] P_n'[\hat{\boldsymbol{n}} \cdot \hat{\boldsymbol{d}}]\, \hat{\boldsymbol{d}} + \tilde{\alpha}(-1)^n (2n+1) \left(\frac{a}{R}\right)^{n+1} P_n'[\hat{\boldsymbol{n}} \cdot \hat{\boldsymbol{R}}]\, \hat{\boldsymbol{R}} \right) \cdot \left(\mathbb{I} - \hat{\boldsymbol{n}}\hat{\boldsymbol{n}}\right) \tag{S13}$$

The total slip velocity is composed of two terms:

$$\boldsymbol{u}_a = -2U_0 \frac{b[\hat{\boldsymbol{n}}]}{b_e} \sum_{n\geq 1} \frac{1}{n+1} \left(K_n[\chi] P_n'[\hat{\boldsymbol{n}} \cdot \hat{\boldsymbol{d}}]\, \hat{\boldsymbol{d}} \right) \cdot \left(\mathbb{I} - \hat{\boldsymbol{n}}\hat{\boldsymbol{n}}\right) \tag{S14}$$

which is solely due to the intrinsic activity of the Janus particle and,

$$\boldsymbol{u}_{sin} = -2U_0 \frac{b[\hat{\boldsymbol{n}}]}{b_e} \sum_{n\geq 1} \frac{1}{n+1} \left(\tilde{\alpha}(-1)^n (2n+1) \left(\frac{a}{R}\right)^{n+1} P_n'[\hat{\boldsymbol{n}} \cdot \hat{\boldsymbol{R}}]\, \hat{\boldsymbol{R}} \right) \cdot \left(\mathbb{I} - \hat{\boldsymbol{n}}\hat{\boldsymbol{n}}\right) \tag{S15}$$

which arises due to the presence of the singularity.

The translational velocity for a spherical Janus particle in an unbounded fluid is given by

$$\boldsymbol{U} = -\frac{1}{4\pi} \int_s \boldsymbol{u}_s dS = -\frac{1}{4\pi} \int_s [\boldsymbol{u}_a + \boldsymbol{u}_{sin}] dS = \boldsymbol{U}_a + \boldsymbol{U}_{sin}. \tag{S16}$$

Assuming, without loss of generality, that $\hat{\boldsymbol{d}} = \hat{\boldsymbol{z}}$ such that $\hat{\boldsymbol{n}} = \sin\theta\cos\phi\hat{\boldsymbol{x}} + \sin\theta\cos\phi\hat{\boldsymbol{y}} + \cos\theta\hat{\boldsymbol{z}}$, the component of the translational velocity due to the intrinsic activity of the particle is given by

$$\boldsymbol{U}_a = \frac{1}{2\pi} U_0 \sum_{n\geq 1} \frac{K_n[\chi]}{(n+1)} \int_0^{2\pi} \int_{-1}^{1} \frac{b[\hat{\boldsymbol{n}}]}{b_e} \big(\hat{\boldsymbol{d}} - \cos\theta \hat{\boldsymbol{n}}\big) P_n'[\cos\theta] d(\cos\theta) d\phi = U_0 \hat{\boldsymbol{d}} \Big(1 + \chi - (1-\beta) B[\chi]\Big), \tag{S17}$$

where

$$B[\chi] = \sum_{n\geq 1} \frac{K_n[\chi]}{(n+1)} \bigg(\big(1 - \chi^2\big) P_n[-\chi] + \int_{-1}^{-\chi} 2u P_n[u] du \bigg). \tag{S18}$$

Again without loss of generality, we assume that $\hat{\boldsymbol{R}} = \hat{\boldsymbol{z}}$, the component of the translational velocity due to the presence of the source can be written as

$$\boldsymbol{U}_{sin} = \frac{1}{2\pi} \tilde{\alpha} U_0 \sum_{n\geq 1} (-1)^n \frac{2n+1}{n+1} \left(\frac{a}{R}\right)^{n+1} \int_0^{2\pi} \int_{-1}^{1} \frac{b[\hat{\boldsymbol{n}}]}{b_e} \, \big(\hat{\boldsymbol{R}} - \hat{\boldsymbol{n}} \cos\theta\big) P_n'[\cos\theta] d(\cos\theta) d\phi \tag{S19}$$

Simplifying the integration in Eq. (S19) to

$$\begin{aligned}
&\int_0^{2\pi} \int_{-1}^{1} \frac{b[\hat{\boldsymbol{n}}]}{b_e} \, \big(\hat{\boldsymbol{R}} - \hat{\boldsymbol{n}} \cos\theta\big) P_n'[\cos\theta] d(\cos\theta) d\phi \\
&= \int_0^{2\pi} \int_{-1}^{1} \big(\hat{\boldsymbol{R}} - \hat{\boldsymbol{n}} \cos\theta\big) P_n'[\cos\theta] d(\cos\theta) d\phi \\
&- (1-\beta) \int_0^{2\pi} \int_{-1}^{1} H[-\hat{\boldsymbol{n}} \cdot \hat{\boldsymbol{d}} - \chi] \big(\hat{\boldsymbol{R}} - \hat{\boldsymbol{n}} \cos\theta\big) P_n'[\cos\theta] d(\cos\theta) d\phi \\
&= \Big(1 - \frac{1}{2}(1-\beta)(1-\chi)\Big) \frac{8\pi}{3} \delta_{n,1} \hat{\boldsymbol{R}} \\
&+ \frac{1}{2}(1-\beta)(1-\chi) \sum_{l\geq 1} K_l[\chi] \int_0^{2\pi} \int_{-1}^{1} P_l[\hat{\boldsymbol{n}} \cdot \hat{\boldsymbol{d}}] \big(\hat{\boldsymbol{R}} - \hat{\boldsymbol{n}} \cos\theta\big) P_n'[\cos\theta] d(\cos\theta) d\phi.
\end{aligned} \tag{S20}$$

The last line follows from applying the Heaviside function expansion given in Eq. (S11). We are able to further simplify Eq. (S20) and find its projection along $\hat{\boldsymbol{R}}$ and $\hat{\boldsymbol{\varphi}}$ by expanding $P_l[\hat{\boldsymbol{n}} \cdot \hat{\boldsymbol{d}}]$ in terms of associated Legendre polynomials $P_n^m[x]$. If we consider the general case where $\boldsymbol{R}$ and $\hat{\boldsymbol{d}}$ are not in the same plane such that $\hat{\boldsymbol{d}}$ and $\hat{\boldsymbol{n}}$ have polar and azimuthal angles Θ and ϕ', and θ and ϕ, respectively, i.e., $\hat{\boldsymbol{d}} = \cos\Theta \hat{\boldsymbol{z}} + \sin\Theta \cos\phi' \hat{\boldsymbol{x}} + \sin\Theta \sin\phi' \hat{\boldsymbol{y}}$, and $\hat{\boldsymbol{n}} = \cos\theta\hat{\boldsymbol{z}} + \sin\theta\cos\phi\hat{\boldsymbol{x}} + \sin\theta\sin\phi\hat{\boldsymbol{y}}$, then

$$P_l[\hat{\boldsymbol{n}}\cdot\hat{\boldsymbol{d}}] = \sum_{m=-l}^{l}\frac{(l-m)!}{(l+m)!}P_l^m[\cos\Theta]P_l^m[\cos\theta]e^{-im\phi'}e^{im\phi}\,. \tag{S21}$$

Upon substitution of Eq. (S21) into Eq. (S20), we obtain

$$\begin{aligned}
&\int_0^{2\pi}\int_{-1}^{1}P_l[\hat{\boldsymbol{n}}\cdot\hat{\boldsymbol{d}}]\big(\hat{\boldsymbol{R}}-\hat{\boldsymbol{n}}\cos\theta\big)P_n'[\cos\theta]d(\cos\theta)d\phi\\
&=\sum_{m=-l}^{l}\frac{(l-m)!}{(l+m)!}P_l^m[\cos\Theta]e^{-im\phi'}\int_0^{2\pi}\int_{-1}^{1}P_l^m[\cos\theta]\big(\hat{\boldsymbol{R}}-\hat{\boldsymbol{n}}\cos\theta\big)P_n'[\cos\theta]e^{im\phi}d(\cos\theta)d\phi\\
&=2\pi P_l[\cos\Theta]\int_{-1}^{1}\big(1-\cos^2\theta\big)P_l[\cos\theta]P_n'[\cos\theta]d(\cos\theta)\hat{\boldsymbol{R}}\\
&\quad-\frac{(l-m)!}{(l+m)!}P_l^m[\cos\Theta]e^{-im\phi'}\pi\int_{-1}^{1}\cos\theta\sin\theta P_l^m[\cos\theta]P_n'[\cos\theta]d(\cos\theta)(\delta_{m,1}+\delta_{m,-1})\big(\hat{\boldsymbol{x}}+im\hat{\boldsymbol{y}}\big)\\
&=2\pi P_l[\cos\Theta]\frac{n(n+1)}{2n+1}\frac{2}{2l+1}(\delta_{l,n-1}-\delta_{l,n+1})\hat{\boldsymbol{R}}+2\pi P_l^1[\cos\Theta]\frac{1}{2n+1}\frac{2}{2l+1}\big(n\delta_{l,n+1}+(n+1)\delta_{l,n-1}\big)\hat{\boldsymbol{\varphi}}.
\end{aligned} \tag{S22}$$

We can now write $\boldsymbol{U}_{sin}$ in terms of $\boldsymbol{R}$ and $\boldsymbol{\varphi}$ by substituting Eq. (S22) into Eq. (S20) and substituting the resulting expression into Eq. (S19) to obtain

$$\boldsymbol{U}_{sin} = U_0\tilde{\alpha}\Big(-2\frac{a^2}{R^2}+(1-\beta)M[\chi,\boldsymbol{R},\hat{\boldsymbol{d}}]\Big)\hat{\boldsymbol{R}} - U_0\tilde{\alpha}(1-\beta)\sin\Theta N[\chi,\boldsymbol{R},\Theta]\hat{\boldsymbol{\varphi}}, \tag{S23}$$

where, $M[\chi,\boldsymbol{R},\Theta]$ and $N[\chi,\boldsymbol{R},\Theta]$ are given by

$$M[\chi,\boldsymbol{R},\Theta] = \frac{a^2}{R^2}(1-\chi)\Big(1-\frac{1}{4}\chi(1+\chi)(3\cos^2\Theta-1)\Big)+(1-\chi)\sum_{n\geq 2}\Big(\frac{a}{R}\Big)^{n+1}\Big(nA_{n+1}-nA_{n-1}\Big), \tag{S24a}$$

$$N[\chi,\boldsymbol{R},\Theta] = -\frac{3}{4}\frac{a^2}{R^2}\chi(1-\chi^2)\cos\Theta-(1-\chi)\sum_{n\geq 2}\frac{1}{n+1}\Big(\frac{a}{R}\Big)^{n+1}\frac{d}{d(\cos\Theta)}\Big(nA_{n+1}+(n+1)A_{n-1}\Big), \tag{S24b}$$

and

$$A_n = \frac{1}{2n+1}(-1)^n P_n[\cos\Theta]K_n[\chi].$$

The total translation velocity [Eq. (7a,b) of the main text] is given by $\boldsymbol{U} = \boldsymbol{U}_a + \boldsymbol{U}_{sin}$.

Prior to calculating the angular velocity of a particle in the presence of a point singularity, we recapitulate a useful result derived in Ref.[2] With the aid of the vector calculus identity $\int_s \hat{\boldsymbol{n}} \times \nabla(b[\hat{\boldsymbol{n}}]C)\ dS = \int \nabla \times \nabla(b[\hat{\boldsymbol{n}}]C)dV = 0$, we can write the angular velocity as

$$\begin{aligned}
\boldsymbol{\Omega} &= -\frac{3}{8\pi a}\int_s \hat{\boldsymbol{n}} \times \boldsymbol{u}_s dS \\
&= -\frac{3}{8\pi a}\int_s -\hat{\boldsymbol{n}} \times b[\hat{\boldsymbol{n}}]\nabla C\ dS \\
&= -\frac{3}{8\pi a}\int_s C\ \hat{\boldsymbol{n}} \times \nabla b[\hat{\boldsymbol{n}}] + \frac{3}{8\pi a}\int_s \hat{\boldsymbol{n}} \times \nabla(b[\hat{\boldsymbol{n}}]C)\ dS \\
&= -\frac{3}{8\pi a^2}b_e(1-\beta)\int_s (C\delta[\hat{\boldsymbol{n}}\cdot\hat{\boldsymbol{d}} + \chi]\ \hat{\boldsymbol{n}} \times \hat{\boldsymbol{d}})\ dS \\
&= \frac{3}{8\pi a^2}b_e(1-\beta)\int_{\hat{\boldsymbol{n}}\cdot\hat{\boldsymbol{d}}=-\chi} C\ \hat{\boldsymbol{d}} \times \hat{\boldsymbol{n}}\ dl.
\end{aligned} \tag{S25}$$

Interestingly, the angular velocity of a spherical particle with bilateral Janus symmetry is proportional to $1-\beta$ and is simply the vector cross product $C\ \hat{\boldsymbol{d}} \times \hat{\boldsymbol{n}}$ along the contour separating the emitting and absorbing region of the particle (i.e., $\hat{\boldsymbol{n}}\cdot\hat{\boldsymbol{d}} = -\chi$). It is straightforward to show for spherical particle with bilateral symmetry the contribution to the angular velocity from the intrinsic activity of the particle is zero:

$$\begin{aligned}
\boldsymbol{\Omega}_a &= -\frac{3}{8\pi a^2}b_e(1-\beta)\int_s C_a\ \delta[\hat{\boldsymbol{n}}\cdot\hat{\boldsymbol{d}} + \chi]\ \hat{\boldsymbol{n}} \times \hat{\boldsymbol{d}}\ d\Omega \\
&= -\frac{3}{4\pi a}U_0(1-\beta)\sum_{n\geq 1}\frac{(1-\chi)K_n[\chi]}{n+1}P_n(-\chi)\int_s \delta[\hat{\boldsymbol{n}}\cdot\hat{\boldsymbol{d}} + \chi]\ \hat{\boldsymbol{n}}\ d\Omega \times \hat{\boldsymbol{d}} = 0.
\end{aligned} \tag{S26}$$

This results of $\boldsymbol{\Omega}_a = 0$ is valid for all phoretic mobility ratios β and Janus balances χ. The contribution to the angular velocity due to the presence of the singularity is given by

$$\begin{aligned}\boldsymbol{\Omega}_{sin} &= -\frac{3}{8\pi a^2} b_e (1-\beta) \int_s (C_{sin} + C_d)\ \delta[\hat{\boldsymbol{n}} \cdot \hat{\boldsymbol{d}} + \chi]\ \hat{\boldsymbol{n}} \times \hat{\boldsymbol{d}}\ d\Omega \\ &= -\frac{3}{4\pi a} U_0 (1-\beta) \tilde{\alpha} \sum_{n\geq 0} (-1)^n \frac{2n+1}{n+1} \left(\frac{a}{R}\right)^{n+1} \int_s P_n[\hat{\boldsymbol{R}} \cdot \hat{\boldsymbol{n}}] \delta[\hat{\boldsymbol{n}} \cdot \hat{\boldsymbol{d}} + \chi]\ \hat{\boldsymbol{n}}\ d\Omega \times \hat{\boldsymbol{d}}.\end{aligned} \tag{S27}$$

The integration in Eq. (S27) can be simplified using a similar procedure as done for the translation velocity, where we first assume, without loss of generality, that $\hat{\boldsymbol{d}} = \hat{\boldsymbol{z}}$, and thus $\hat{\boldsymbol{n}} = \cos\theta \hat{\boldsymbol{z}} + \sin\theta \cos\phi \hat{\boldsymbol{x}} + \sin\theta \sin\phi \hat{\boldsymbol{y}}$ and $\hat{\boldsymbol{R}} = \cos\Theta\ \hat{\boldsymbol{z}} + \sin\Theta \cos\phi'\ \hat{\boldsymbol{x}} + \sin\Theta \sin\phi'\ \hat{\boldsymbol{y}}$. We then write $P_n[\hat{\boldsymbol{R}} \cdot \hat{\boldsymbol{n}}]$ in terms of associated Legendre polynomials $P_n^m[x]$ where the integration in Eq. (S27) simplifies to

$$\begin{aligned}&\int_s P_n[\hat{\boldsymbol{R}} \cdot \hat{\boldsymbol{n}}] \delta[\hat{\boldsymbol{n}} \cdot \hat{\boldsymbol{d}} + \chi]\ \hat{\boldsymbol{n}}\ d\Omega \times \hat{\boldsymbol{d}} \\ &= \sum_{m=-n}^{n} \frac{(n-m)!}{(n+m)!} P_n^m[\cos\Theta] e^{-im\phi'} \int_0^{2\pi} \int_0^{\pi} e^{im\phi} P_n^m[\cos\theta] \hat{\boldsymbol{n}} \delta[\cos\theta + \chi] \sin\theta d\theta d\phi \times \hat{\boldsymbol{d}} \\ &= \sum_{m=-n, n\neq 0}^{n} \pi\,(1-\chi^2) \frac{(n-m)!}{(n+m)!} P_n^m[\cos\Theta] P_n^m[-\chi] e^{-im\phi'} \Big((\delta_{m,1} + \delta_{m,-1})(\hat{\boldsymbol{x}} + im\hat{\boldsymbol{y}}) \Big) \times \hat{\boldsymbol{d}} \\ &= 2\pi(1-\chi^2) \frac{(n-1)!}{(n+1)!} P_n^1[\cos\Theta] P_n^1[-\chi] \big(\cos\phi' \hat{\boldsymbol{x}} + \sin\phi' \hat{\boldsymbol{y}} \big) \times \hat{\boldsymbol{d}} \\ &= \frac{2\pi(1-\chi)\sqrt{1-\chi^2}}{2n+1} \sin\Theta \frac{dP_n[\cos\Theta]}{d(\cos\Theta)} K_n[\chi]\ \frac{\hat{\boldsymbol{R}} \times \hat{\boldsymbol{d}}}{|\hat{\boldsymbol{R}} \times \hat{\boldsymbol{d}}|}.\end{aligned} \tag{S28}$$

The integration result from Eq. (S28) can be substituted into Eq. (S27) to obtain the expression in the main text [Eq. (7c)] for the total angular velocity:

$$\boldsymbol{\Omega} = -\frac{3U_0\tilde{\alpha}}{2a} (1-\beta) \sin\Theta\ \omega[\chi, \boldsymbol{R}, \hat{\boldsymbol{d}}]\ \frac{\hat{\boldsymbol{R}} \times \hat{\boldsymbol{d}}}{|\hat{\boldsymbol{R}} \times \hat{\boldsymbol{d}}|}, \tag{S29}$$

where

$$\omega[\chi, \boldsymbol{R}, \Theta] = \sqrt{1-\chi^2}(1-\chi)\sum_{n\geq 1}(-1)^n \frac{1}{n+1}\left(\frac{a}{R}\right)^{n+1} \frac{dP_n[\cos\Theta]}{d(\cos\Theta)} K_n[\chi]. \tag{S30}$$

Lastly, we note the angular velocity is only non-zero in the direction perpendicular to $\hat{\boldsymbol{d}}$ and $\boldsymbol{R}$, restricting the motion of the particle to the two dimensional plane containing the particle orientation $\hat{\boldsymbol{d}}$ and radial vector $\hat{\boldsymbol{R}}$.

Radial dependence of dimensionless parameters $B[\chi]$, $M[\chi, R, \Theta], N[\chi, R, \Theta]$, and $\omega[\chi, R, \Theta]$ for $\chi = 0$

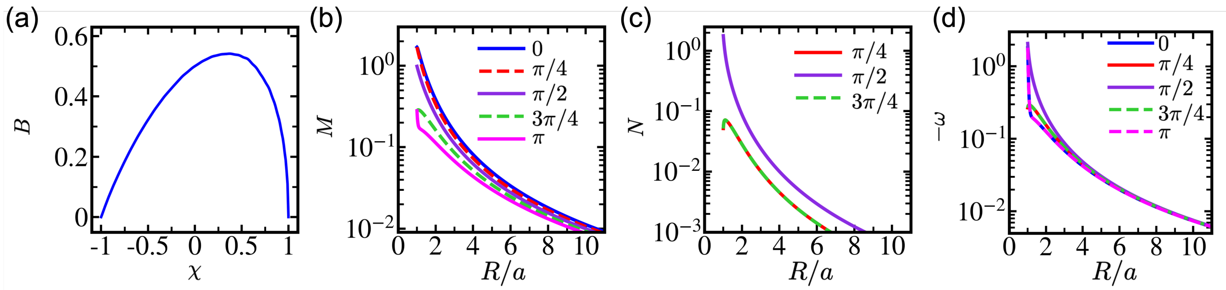

Figure S1: (a) Parameter $B[\chi]$ as a function of Janus-balance χ. (b–d) Parameters $M[\chi, R, \Theta]$, $N[\chi, R, \Theta]$, and $\omega[\chi, R, \Theta]$ for $\chi = 0$ for different orientations Θ as a function of the radial distance from the singularity. Note that $N[\chi, R, \Theta]$ vanishes for $\Theta = 0$ and π.

Simulation Details

We employ an explicit Euler scheme to integrate the particle's equations of motion (Eq. (1) of the main text). For a given initial position R_0 and orientation Θ_0 of the particle, the trajectory is computed via

$$R_{i+1} = R_i + U_R(R_i, \Theta_i)dt, \tag{S31a}$$

$$\varphi_{i+1} = \varphi_i + \frac{U_\varphi(R_i, \Theta_i)}{R_i}dt, \tag{S31b}$$

$$\gamma_{i+1} = \gamma_i + \Omega_z(R_i, \Theta_i)dt, \tag{S31c}$$

$$\Theta_i = \gamma_i - \varphi_i. \tag{S31d}$$

The velocities are calculated at each timestep via the analytical expression derived above with the various infinite summations truncated at 400 terms. The Legendre polynomials were evaluated using the 'scipy.special. eval_legendre' function from the 'scipy' Python library. The accuracy of the analytical solution and its truncation were validated using Boundary Element Method (BEM) simulations to determine the particle velocity. This process involves solving the Laplace and Stokes equations in three dimensions, utilizing BEMLIB codes implemented in FORTRAN[3] and specifically adapted for an active Janus particle.[4,5] All BEM results agreed with the analytical solution [Eq. (8)] and its truncated form.

Location of fixed points as a function of the strength of the singularity

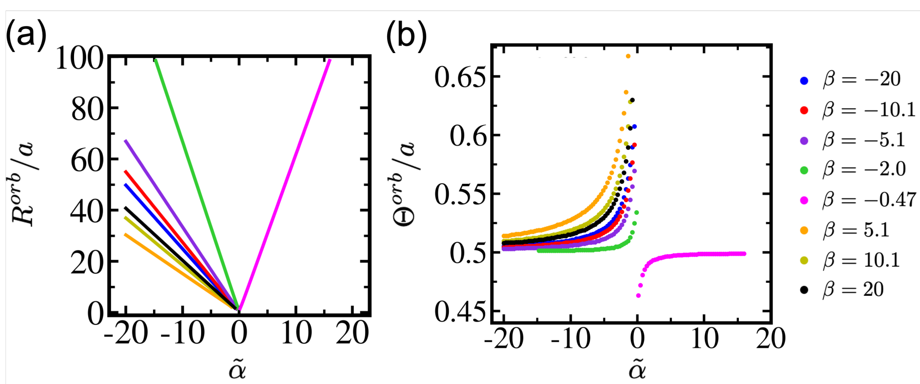

Figure S2: The radial R^{orb}/a and orientation Θ^{orb} dependence of orbiting states as a function of the strength of the singularity $\tilde{\alpha}$ for different phoretic mobility ratios β. As the strength of the singularity increases, orbiting states occur further from the singularity, and the orientation asymptotically approaches an angle of $\Theta^{orb} = \pi/2$.

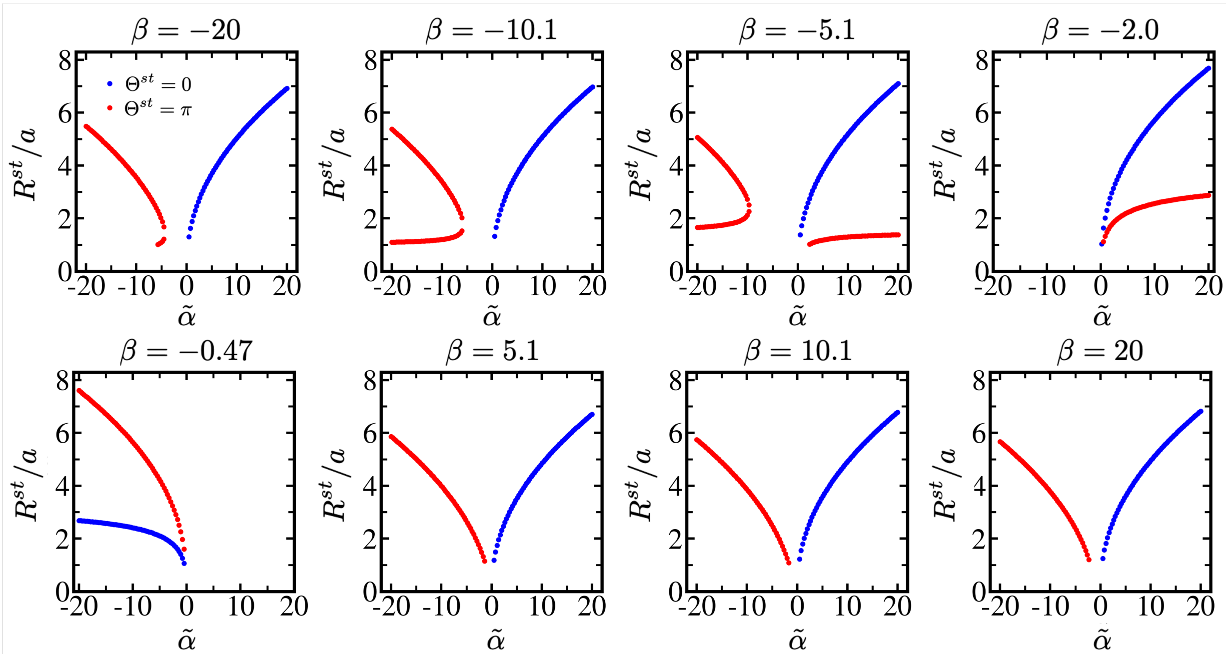

Figure S3: The radial dependence of stationary states R^{st}/a with orientations $\Theta^{st} = 0$ (blue) and π (red) as a function of the strength of the singularity $\tilde{\alpha}$ for various phoretic mobility ratios β. The general trend is that as the singularity's strength increases, the fixed points occur further away from the singularity. For $\Theta = 0$, stationary states occur exclusively in the presence of a point source ($\tilde{\alpha} > 0$) for all phoretic mobility ratios β, except in interval $-1 < \beta < 0$ where the stationary state arise in the presence of a point source. For $\beta = -10.1$ and $\beta = -5.1$, there are two stationary states for $\Theta = \pi$ for a broad range of $\tilde{\alpha}$. As the strength of the sink decreases, these two branches of stationary states converge to a single stationary stare before disappearing entirely.

Details of Simulation Videos

Each movie shows the real-space trajectory for the different values of the phoretic mobility ratio in Figures 3, 4, and 5 of the main text. The trajectory colors are consistent with those shown in the figures, and the vector corresponds to the orientation Θ. The singularity is represented as a grey circle, and the time is given in units of $a/U_0 = 2aD/(Q_e b_e)$.

1. `video_1(fig3a).mp4` – $U_0 = 1$, $\tilde{\alpha} = 10$ and $\beta = -10$
2. `video_2(fig3b).mp4` – $U_0 = 1$, $\tilde{\alpha} = 10$ and $\beta = -2$
3. `video_3(fig3c).mp4` – $U_0 = 1$, $\tilde{\alpha} = 10$ and $\beta = 0$
4. `video_4(fig3d).mp4` – $U_0 = 1$, $\tilde{\alpha} = 10$ and $\beta = 5$
5. `video_5(fig4a).mp4` – $U_0 = 1$, $\tilde{\alpha} = -10$ and $\beta = -15$
6. `video_6(fig4b).mp4` – $U_0 = 1$, $\tilde{\alpha} = -10$ and $\beta = -8$
7. `video_7(fig4c).mp4` – $U_0 = 1$, $\tilde{\alpha} = -10$ and $\beta = -2$
8. `video_8(fig4d).mp4` – $U_0 = 1$, $\tilde{\alpha} = -10$ and $\beta = -0.5$
9. `video_9(fig4e).mp4` – $U_0 = 1$, $\tilde{\alpha} = -10$ and $\beta = 10$
10. `video_10(fig5).mp4` – $U_0 = -1$, $\tilde{\alpha} = 10$ and $\beta = 0.644$

References

(1) Bayati, P.; Popescu, M. N.; Uspal, W. E.; Dietrich, S.; Najafi, A. Dynamics Near Planar Walls for Various Model Self-Phoretic Particles. *Soft matter* **2019**, *15*, 5644–5672.

(2) Popescu, M. N.; Uspal, W. E.; Bechinger, C.; Fischer, P. Chemotaxis of Active Janus Nanoparticles. *Nano Lett.* **2018**, *18*, 5345–5349.

(3) Pozrikidis, C. *A Practical Guide to Boundary Element Methods With the Software Library BEMLIB*; CRC Press, 2002.

(4) Uspal, W.; Popescu, M. N.; Dietrich, S.; Tasinkevych, M. Self-Propulsion of a Catalytically Active Particle Near a Planar Wall: From Reflection to Sliding and Hovering. *Soft Matter* **2015**, *11*, 434–438.

(5) Bayati, P.; Najafi, A. Dynamics of Two Interacting Active Janus Particles. *J. Chem. Phys.* **2016**, *144*, 134901.